Absolute static-field magnetometry, magnetic gradiometry, and vector electrometry with circular Rydberg atoms

Junwen Zou and Stephen D. Hogan*
Department of Physics and Astronomy, University College London, Gower Street, London WC1E 6BT, United Kingdom

(Received 3 April 2023; accepted 2 June 2023; published 26 June 2023)

Helium atoms in pulsed supersonic beams have been prepared in the circular Rydberg state with principal quantum number $n = 55$ using the crossed-fields method. High-resolution microwave spectroscopy of the transition from this state to the $n = 56$ circular state, at frequencies close to 38.5 GHz, was performed to measure static magnetic and electric fields along the axis of propagation of the beams with quantum-state-selective detection by pulsed-electric-field ionization. Magnetic fields of between 1.3 and 1.6 mT were measured to a relative precision of ±900 nT by rf spectroscopy and ±1.3 μT by microwave spectroscopy, with absolute calibration, accounting for Doppler shifts and effects of weak stray electric fields to ±2.0 μT and a spatial resolution of ±0.87 mm. Magnetic-field gradients could be determined to a precision of ±1.49 μT/mm (±53 nT/mm) over a baseline of 1.74 mm (35 mm). To perform these measurements, static electric fields and contributions from the motional Stark effect were minimized, and residual electric fields in each of the three spatial dimensions in the apparatus were measured to an absolute precision of between ±85 and ±750 μV/cm. The methods used in this work can be transferred to experiments with other atoms or molecules. They are therefore well suited for applications in minimally invasive, absolute static-field magnetometry and electrometry, for example, at hybrid interfaces between Rydberg atoms and superconducting circuits; in tests of bound-state QED or the weak equivalence principle with atomic or molecular hydrogen, antihydrogen, or positronium; and in measurements of the absolute neutrino mass by cyclotron radiation emission spectroscopy.

DOI: 10.1103/PhysRevA.107.062820

I. INTRODUCTION

Atoms in Rydberg states with high principal quantum number n can act as sensitive microscopic probes of static magnetic and electric fields that cause minimal disturbance to their local electromagnetic environment. Rydberg-atom magnetometers have been demonstrated with rubidium atoms, which allowed single-shot detection of static magnetic fields as small as 13 nT [1]. Measurements of static electric fields to a precision of 20 μV/cm have been performed by high-resolution millimeter-wave spectroscopy of Rydberg-Rydberg transitions in krypton [2]. Rydberg atoms can also be employed to measure time-varying electromagnetic fields. They are widely used in the implementation of optical quantum sensors for radio-frequency, microwave, and terahertz radiation [3,4]. In all of these cases, absolute field strengths can be determined without regular calibration. This is because the energy-level structure and Zeeman and Stark shifts, including ac Stark shifts, of the Rydberg states can be accurately calculated to high precision.

Since all atoms and molecules with a stable ion core possess Rydberg states, methods for magnetometry and electrometry involving these states can in general be readily transferred from one species to another. This is most evident for measurement schemes involving circular Rydberg states. These states have maximal electron orbital angular momentum and magnetic quantum numbers ℓ and m_ℓ, respectively, for a particular value of n, i.e., $|m_\ell| = \ell = n - 1$ [5,6]. Atoms in circular Rydberg states have long lifetimes (greater than 30 ms for values of $n > 50$), strong electric dipole transitions at radio and microwave frequencies (greater than $1000ea_0$ for $\Delta n = +1$ transitions between circular states with values of $n > 50$), low static electric dipole polarizabilities, and comparatively large magnetic dipole moments (greater than $49\,\mu_B$ for values of $n > 50$). The restrictions imposed by the selection rules for single-photon electric dipole transitions involving one individual Rydberg electron, i.e., that $\Delta\ell = \pm 1$ and $\Delta m_\ell = 0, \pm 1$, and parity must change, mean that pairs of circular Rydberg states which differ in their values of n by 1 can act as quasi-two-level systems. Because of this, these states are of importance in microwave cavity quantum electrodynamics experiments [7,8], high-precision spectroscopy [9–11], and the development of new techniques for quantum sensing [1,12] including by matter-wave interferometry [13]. Work is also currently underway to implement quantum simulators with atoms in circular Rydberg states [14].

The reason the properties and characteristics of circular Rydberg states do not depend strongly on atomic species is that the centrifugal barrier, experienced by the single

*s.hogan@ucl.ac.uk

excited electron in such a state, is sufficiently large that it inhibits penetration into the region close to the ion core. Consequently, deviations of the charge distribution of the core from a pure Coulomb potential at short range do not significantly perturb the electron. The experimental methods, sensitivity, and measurement precision achieved in magnetometers and electrometers based on circular Rydberg states can therefore be directly transferred from one species to another. This allows optimal species to be selected to match the requirements, or constraints, of any particular measurement environment.

In the high-vacuum, and often cryogenic, environments of hybrid cavity QED experiments with Rydberg atoms and superconducting circuits [15,16]; precision spectroscopy experiments directed toward tests of bound state QED or the weak equivalence principle with atomic [17,18] or molecular hydrogen [19], antihydrogen [20] or positronium [21–23]; or in experiments to measure the absolute neutrino mass by electron cyclotron radiation emission spectroscopy (CRES) following beta decay of tritium atoms [24,25], it is essential to avoid introducing contaminants into the apparatus, e.g., polarizable, heavy rare-gas atoms, alkali-metal atoms, or polar molecules, that could be adsorbed on cold surfaces and become a source of stray electric fields that change over time [26]. In these settings, the optimal atomic quantum sensors for magnetometry and electrometry are those already present in the apparatus for the measurements, or species that are inert or will cause minimal contamination, and will not freeze on the cryogenic surfaces, e.g., atomic hydrogen or helium. By allowing beams of these atoms, prepared in circular Rydberg states, to propagate in a controlled way through the part of the experimental apparatus in which the magnetic and electric fields are to be characterized, high-precision absolute sensing can be performed.

The absolute *in situ* measurement of static electric fields, to a precision better than the 1 mV/cm reported here and required for many of the above applications, cannot be easily performed with sensors other than Rydberg atoms. High-precision absolute, i.e., ±46 nT, measurements of static magnetic fields could be carried out by alternative means, e.g., by ^{3}He nuclear magnetic resonance methods [27]. However, this can be challenging to implement over a large measurement volume within a cryogenic apparatus and cannot be exploited to measure electric fields which is crucial, for example, in experiments to determine the absolute neutrino mass by CRES. The opportunity to use atoms in circular Rydberg states for combined electric- and magnetic-field sensing therefore makes this approach appealing in restrictive experimental environments.

Here we report measurements of absolute static magnetic fields, including magnetic-field gradients, and electric fields using helium atoms in circular Rydberg states. The particular states used had principal quantum numbers $n = 55$ and 56. Measurements were performed by high-resolution microwave spectroscopy of transitions between these circular states at frequencies close to 38.5 GHz and radio-frequency (rf) spectroscopy of the $\Delta n = 0$ and $\Delta m_\ell = -1$ transition from the $n = 55$ circular state at a frequency close to 22 MHz. The experiments were carried out in a pulsed mode. This allowed fields at a range of positions, over a distance of approximately 35 mm along the axis of propagation of the atomic beams, to be mapped by recording spectra at a range of delay times after Rydberg state laser photoexcitation.

The remainder of this article is structured as follows. The apparatus and methods used in the experiments are described in Sec. II. This is followed in Sec. III by a description of the energy-level structure and Stark and Zeeman shifts of the Rydberg states used for magnetometry and electrometry, and the spectral line shapes encountered in the analysis of the experimental data. In Sec. IV the results of the absolute measurements of static magnetic and electric fields are presented. This includes the determination of magnetic-field gradients and the x, y, and z components of stray electric fields. Finally, a summary is given and prospects for future developments and refinements to the measurement schemes are discussed in Sec. V.

II. EXPERIMENTAL SETUP

A schematic diagram of the experimental apparatus is shown in Fig. 1(a). Supersonic beams of He were generated using a water-cooled pulsed valve operated at 290 K. A dc discharge was implemented at the exit of the valve to populate the metastable $1s2s\,^3S_1$ level [28]. The resulting atoms propagated in the y dimension with a longitudinal speed of 1745 ± 50 m/s. After passing through a 2-mm-diameter skimmer and an electrostatic filter to remove charged particles generated in the discharge, the atoms entered a region between two parallel polished copper electrodes E1 and E2 separated in the x dimension by 13.46 ± 0.03 mm. These electrodes were mounted at each corner with ceramic spacers from four aluminium posts. To mitigate the effects of charge buildup on the spacers, there was no line of sight from them to the measurement region. In this part of the apparatus, a magnetic field of $\vec{B} \simeq (0, 0, 1.6)$ mT acting in the z dimension was generated by a pair of solenoids located outside the vacuum chamber and operated in a Helmholtz-type configuration with a current of 12 A. These solenoids each comprised 30 windings of 2.25-mm-diameter multistrand copper wire. They had inner (outer) diameters of 160 mm (180 ± 2 mm). The distance between their inner (outer) edges in the z dimension was 153 ± 3 mm (250 mm).

Between E1 and E2, the atoms crossed two copropagating, frequency-stabilized cw laser beams with wavelengths of 388.975 and 786.755 nm. These had full width at half maximum (FWHM) spectral widths below 5 MHz, were focused to FWHM beam sizes of less than 100 μm, and drove the two-color two-photon $1s2s\,^3S_1 \rightarrow 1s3p\,^3P_2 \rightarrow 1sns/1snd$ excitation scheme [29]. To prepare atoms in the $n = 55$, $\ell = 54$, and $m_\ell = +54$ circular Rydberg state ($|55c\rangle$) using the crossed fields method [30,31], photoexcitation was carried out in an $\vec{F} = (3.21, 0, 0)$ V/cm electric field acting in the x dimension. This allowed efficient and selective excitation of the atoms to the ℓ- and m_ℓ-mixed Stark state that evolves adiabatically to the $|55c\rangle$ state in zero electric field [32]. The excitation electric field was generated by applying a pulsed potential of $V_{\rm ex} = 4.32$ V to E2 for a time $T_{\rm ex} = 1\,\mu$s with E1 set to 0 V [see Fig. 1(b)]. After this, the potential on E2 was reduced to an offset value $V_{\rm off}$ close to zero in a time of $\Delta t_{\rm off} = 1.25\,\mu$s to adiabatically transfer the excited-state

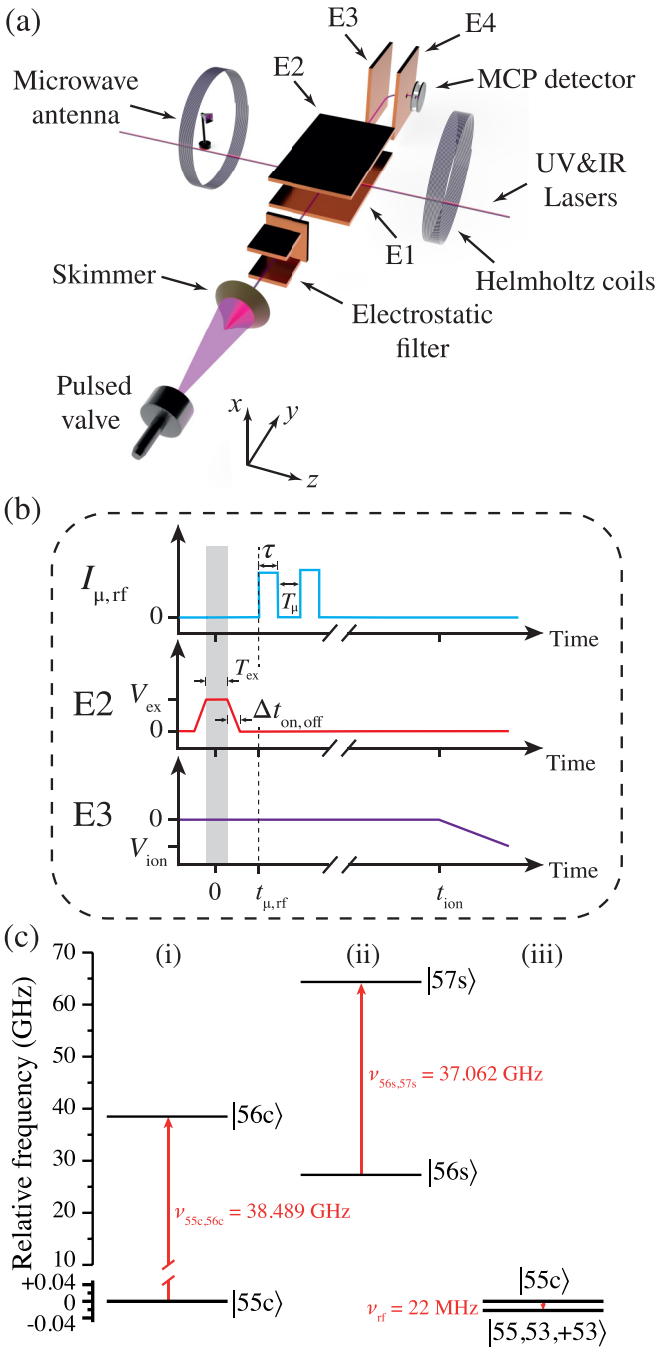

FIG. 1. (a) Schematic diagram of the experimental apparatus. (b) Sequence of pulsed electric potentials and microwave or rf fields used for circular state preparation (E2), microwave or rf spectroscopy ($I_{\mu,\mathrm{rf}}$), and Rydberg-state-selective pulsed-electric-field ionization (E3). (c) Rydberg-Rydberg transitions employed for (i) precision sensing, (ii) characterization of residual uncanceled stray electric fields, and (iii) absolute magnetic-field calibration with minimal first-order Doppler contributions.

population into the $|55c\rangle$ state in zero electric field with an efficiency approaching 100%.

After circular state preparation, the Rydberg atoms were exposed to a sequence of microwave or rf pulses that drove the $\Delta n = +1$ single-photon circular-to-circular state transition, i.e., the $|55c\rangle \rightarrow |56c\rangle$ transition, or the $\Delta n = 0$ and $\Delta m_\ell = -1$ transition from the $|55c\rangle$ state as depicted in Fig. 1(c). The microwave radiation required to drive the $|55c\rangle \rightarrow |56c\rangle$ transition propagated into the measurement region from an antenna located outside the vacuum chamber. Although this field entered the chamber from the direction perpendicular to the axis of propagation of the atomic beam, reflections from the electrode structures onto the beam axis meant that contributions from first-order Doppler shifts could not be neglected. The rf field required to drive the $\Delta n = 0$ and $\Delta m_\ell = -1$ transition was generated by modulating the potential applied to electrode E1. Single-pulse Rabi spectroscopy and double-pulse Ramsey spectroscopy were performed to minimize stray electric fields, cancel the motional Stark effect, and determine transition frequencies to high precision. Measurements were performed at time delays between $t_\mu = 3.15$ and 23.15 μs after laser photoexcitation [see Fig. 1(b)] to characterize fields over a distance of approximately 35 mm along the axis of propagation of the atomic beam.

Following microwave interrogation between E1 and E2, the Rydberg atoms traveled a further 10 cm downstream to the detection region of the apparatus between electrodes E3 and E4. There, Rydberg-state-selective detection was carried out by ionization in a slowly rising pulsed electric field oriented parallel to the background magnetic field. This field was generated by applying a pulsed negative potential to E3 at the time $t_{\mathrm{ion}} = 75$ μs. In this detection geometry, the ionization rate of the $|55c\rangle$ ($|56c\rangle$) state exceeded 10^8 s^{-1} for fields above 98 V/cm (91 V/cm) [33]. Ionized electrons were accelerated through a 13-mm-diameter aperture in the grounded electrode E4 and collected at a microchannel plate (MCP) detector.

III. ENERGY-LEVEL STRUCTURE AND SPECTRAL LINE SHAPES

A. Frequency intervals and transition moments

In the experiments reported here single-photon electric dipole transitions between the $|55c\rangle$ and $|56c\rangle$ states in He were probed by high-resolution microwave spectroscopy at frequencies close to $\nu_{55c,56c} = 38.489$ GHz [Fig. 1(ci)] and transitions between the $|55c\rangle$ state with $m_\ell = +54$ and the $|n, m_\ell\rangle = |55, +53\rangle$ state were measured at radio frequencies around $\nu_{\mathrm{rf}} = 22$ MHz [Fig. 1(cii)]. These transitions have electric dipole transition moments of $|\langle 56c|\mu_{\mathrm{elec}}|55c\rangle| = 2148ea_{\mathrm{He}}$ and $|\langle 55, +53|\mu_{\mathrm{elec}}|55, +54\rangle| = 606ea_{\mathrm{He}}$, respectively ($e$ is the electron charge and a_{He} is the Bohr radius corrected for the reduced mass of He). These transitions, along with the electric dipole forbidden single-photon $1s56s\,^3S_1 \rightarrow 1s57s\,^3S_1$ ($|56s\rangle \rightarrow |57s\rangle$) transition at a frequency of $\nu_{56s,57s} = 37.062$ GHz [Fig. 1(ciii)], allowed the atoms to be exploited as microscopic probes of magnetic and electric fields, and systematic frequency shifts caused by residual uncanceled stray electric fields, and the Doppler effect, to be determined.

Transitions between pairs of circular Rydberg states are well suited for absolute atomic magnetometry because the frequencies at which they occur in the absence of external fields can be calculated to high precision and they do not have significant fine-structure splittings. For example, the spin-orbit splittings of the $|55c\rangle$ and $|56c\rangle$ states used

here are below 1 kHz [34,35]. The Zeeman energy shifts of transitions involving circular Rydberg states can therefore be described analytically to high accuracy, allowing for the straightforward determination of magnetic-field strengths from measured resonance frequencies. The Stark energy shifts of circular Rydberg states in weak electric fields can also be accurately calculated, and if appropriate sets of complementary measurements are made, contributions from Stark and Zeeman shifts can be distinguished.

The measured $|55c\rangle \rightarrow |56c\rangle$ transition frequencies $\nu_{\rm meas}$ can be expressed in a general form as

$$\nu_{\rm meas} = \nu_{55c,56c} + \Delta\nu_{\rm Z} + \Delta\nu_{\rm S} + \Delta\nu_{\rm D}, \tag{1}$$

where $\Delta\nu_{\rm Z}$, $\Delta\nu_{\rm S}$, and $\Delta\nu_{\rm D}$ are the Zeeman, Stark, and Doppler shifts, respectively. If $\Delta\nu_{\rm S}$ and $\Delta_{\rm D}$ are minimized and residual contributions accurately accounted for, the absolute magnetic-field strength B can be determined directly from $\nu_{\rm meas}$.

B. Effects of static electric fields

1. *n*-changing microwave transitions

In a magnetic field $\vec{B} = (0, 0, B_z)$, the Stark shift of a circular Rydberg state depends on the relative orientation of the electric field $\vec{F}$ with respect to the magnetic field. For an electric field oriented perpendicular to the magnetic field, i.e., $\vec{F} = (F_x, 0, 0)$ or $\vec{F} = (0, F_y, 0)$, the combined Zeeman and Stark energy shifts of a circular state in a hydrogenic system with principal quantum number n in weak electric fields can be expressed as [30,36]

$$\Delta E^{\rm (perp)}_{\rm Z,S} = m_\ell \sqrt{(\mu_{\rm B} B_z)^2 + \left(\tfrac{3}{2} n e a_{\rm He} F_x\right)^2}. \tag{2}$$

For $m_\ell = +(n-1)$ the resulting shift is positive and depends quadratically on F_x in weak electric fields. The corresponding shift in the $|55c\rangle \rightarrow |56c\rangle$ transition frequency, $\Delta\nu_{\rm S}$, in a magnetic field of 1.6 mT, as encountered in the experiments reported here, is displayed in Fig. 2(a). In this figure, $\Delta\nu_{\rm S} = +1$ kHz (+10 kHz) when F_x or $F_y = 1.15$ mV/cm (3.65 mV/cm).

The Stark shifts of circular Rydberg states in an electric field $\vec{F} = (0, 0, F_z)$ oriented parallel to a background magnetic field are significantly smaller than those in perpendicular fields. In this case the combined Zeeman and Stark energy shifts are quadratic, negative, and given to second order by [37]

$$\Delta E^{\rm (para)}_{\rm Z,S} = m_\ell \mu_{\rm B} B_z + \cdots - \frac{1}{16} n^4 \left(17n^2 - 9m_\ell^2 + 19\right) \frac{e^2 a_{\rm He}^2}{2hcR_{\rm He}} F_z^2, \tag{3}$$

where $R_{\rm He}$ is the Rydberg constant corrected for the reduced mass of He and h and c are the Planck constant and speed of light in vacuum, respectively. The Stark shift of the $|55c\rangle \rightarrow |56c\rangle$ transition in a 1.6-mT magnetic field and parallel electric fields up to 20 mV/cm is seen in Fig. 2(b). In this case, $\Delta\nu_{\rm S} = -1$ kHz only when $F_z = 49.6$ mV/cm.

The accuracies with which the analytic expressions in Eqs. (2) and (3) can be used to determine the Zeeman and Stark shifts of the $|55c\rangle \rightarrow |56c\rangle$ transition in He were tested by comparison with the results of numerical calculations

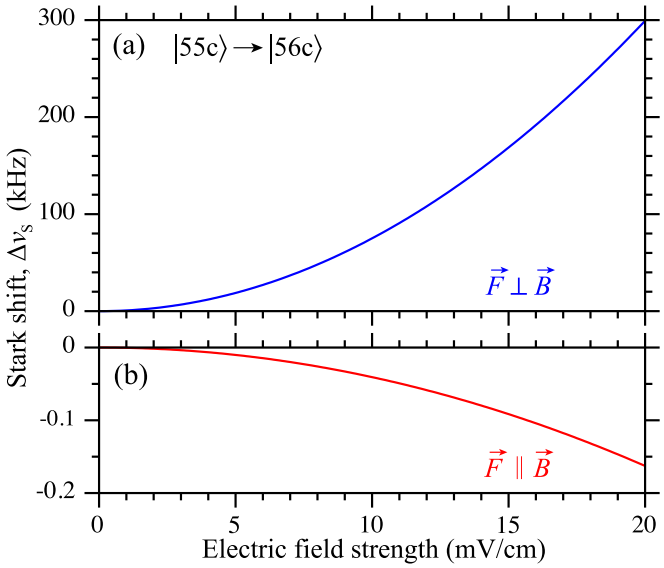

FIG. 2. Stark shift of the $|55c\rangle \rightarrow |56c\rangle$ transition in weak electric fields (a) perpendicular and (b) parallel to a background magnetic field of 1.6 mT

of the eigenvalues of the corresponding Hamiltonian matrix accounting for the nonzero quantum defects of the nonhydrogenic low-ℓ states [34], but excluding spin-orbit contributions. These calculations were performed in an $|n, \ell, m_\ell\rangle$ basis with values of n from 54 to 57 inclusive and all corresponding values of ℓ and m_ℓ [32]. From this comparison, the Stark shifts of this circular-to-circular state transition in a magnetic field of 1.6 mT calculated using the analytic expressions were found to deviate from the numerical results by less than 0.3 kHz for electric fields up to 20 mV/cm. The residual electric fields encountered in the following are all below this value. For reference, a frequency shift on this scale would correspond to an error in the determination of a magnetic-field strength of 20 nT.

2. m_ℓ-changing radio-frequency transitions

Measurements of the $\Delta n = 0$ and $\Delta m_\ell = -1$ transition from a circular state within a single n manifold allow the static electric dipole moments, and therefore the linear Stark shift, of the $m_\ell = +(n-2)$ sublevels in weak electric fields $\vec{F} = (0, 0, F_z)$ oriented parallel to a background magnetic field to be exploited to enhance the electric-field sensitivity of the measurements. In this situation, the Stark shift in a hydrogenic system is given to first order by the expression [37]

$$\Delta E^{\rm (para)}_{\rm Z,S} = \tfrac{3}{2} n k e a_{\rm He} F_z, \tag{4}$$

where the index k is the difference between the quantum numbers n_1 and n_2 associated with the solution of the Schrödinger equation in parabolic coordinates [38,39]. For each set of possible values of n and m_ℓ, the values of k range from $-(n - |m_\ell| - 1)$ to $+(n - |m_\ell| - 1)$ in intervals of 2. For a circular state with $m_\ell = n - 1$, $k = 0$ and there is no first-order Stark shift. However, for a state with $m_\ell = n - 2$ the possible values of k are ± 1. The Stark splitting of the $|55c\rangle = |55, m_\ell = +54\rangle \rightarrow |55, +53\rangle$ transition under these conditions can be

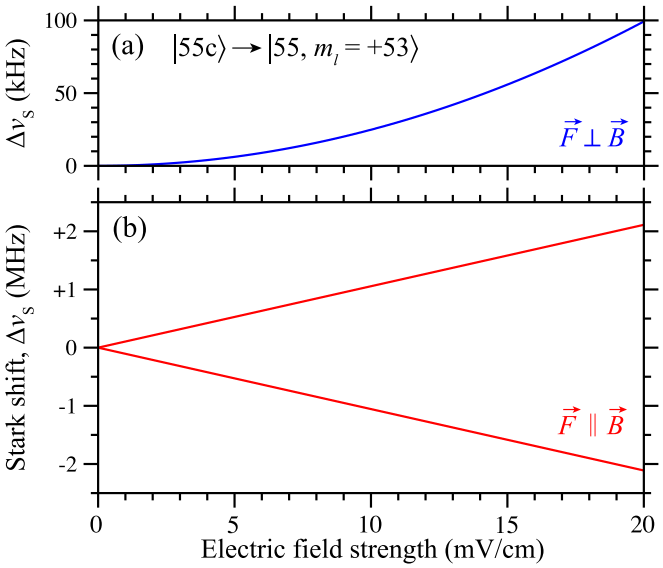

FIG. 3. Stark shift of the $|55c\rangle = |55, m_\ell = +54\rangle \rightarrow |55, +53\rangle$ transition in an electric field (a) perpendicular and (b) parallel to a background magnetic field of 1.6 mT.

seen in Fig. 3(b). In this case, a splitting of 1 kHz (10 kHz) is encountered for an electric field of 5 μV/cm (47 μV/cm). The Stark shift of this rf transition in a perpendicular electric field can be determined using the expression in Eq. (2) and is displayed in Fig. 3(a). In this situation, $\Delta\nu_S = +1$ kHz (+10 kHz) when F_x or $F_y = 2.00$ mV/cm (6.34 mV/cm).

The accuracy with which the Zeeman and Stark shifts of $\Delta n = 0$ and $\Delta m_\ell = -1$ transitions in He are described in weak electric fields by the analytic expressions in Eqs. (2) and (3) was also evaluated by comparison with numerical calculations. For a magnetic field of 1.6 mT, the Stark shifts calculated using the analytic expressions remain within 0.15 kHz of the results of the numerical calculations for electric fields up to 50 mV/cm.

C. Spectral line shapes

The transitions employed in the work reported here were probed using microwave or rf pulse sequences comprising a single pulse with a duration $\tau = 1$ μs or pairs of pulses each with a duration $\tau = 100$ ns and separated by a free-evolution time $T_\mu = 800$ ns. For atoms initially in the $|55c\rangle$ state, the single-pulse measurements resulted in spectral features, recorded, e.g., by monitoring population transfer to the $|56c\rangle$ state, $P_{56c}(\nu_\mu)$, described by a sinc-squared or Rabi line-shape function [40]

$$P_{56c}(\nu_\mu) = A\,\frac{\sin^2(\Delta\tau/2)}{(\Delta\tau/2)^2}, \tag{5}$$

where $\Delta = 2\pi \times (\nu_\mu - \nu_0)$, with ν_μ and ν_0 the frequency of the microwave field and the resonance frequency, respectively, and A is a constant that depends on the Rabi frequency at which the transition is driven.

Neglecting the effects of decoherence, spectra recorded with pairs of microwave pulses separated by the free-evolution time T_μ exhibit a Ramsey line shape given by [41]

$$P_{56c}(\nu_\mu) = B\frac{\sin^2(\Delta\tau/2)}{(\Delta\tau/2)^2}\,\cos^2\left(\frac{\Delta T_\mu}{2}\right), \tag{6}$$

where B is a constant. In the Ramsey spectra reported here, minor contributions from decoherence of the atomic superpositions states in the free-evolution time between the pairs of microwave pulses were evident. This slightly reduced the contrast of the Ramsey fringes represented by the $\cos^2$ term in Eq. (6) to below unity. To account for this in the line-shape function, an exponential damping with a coherence time constant $T_{\rm coh}$ was introduced such that

$$P_{56c}(\nu_\mu) = C\,\frac{\sin^2(\Delta\tau_{\rm p}/2)}{(\Delta\tau_{\rm p}/2)^2} \times \cdots \times\left\{\left[\cos^2\left(\frac{\Delta T}{2}\right) - \frac{1}{2}\right]e^{-T/T_{\rm coh}} + \frac{1}{2}\right\}. \tag{7}$$

To determine resonance frequencies from the measured spectra, the appropriate line-shape functions were fit to the experimental data using least-squares methods. For the fixed total interrogation time of 1 μs in all measurements, chosen to maintain a balance between the absolute precision with which electric and magnetic fields could be determined and the achievable spatial resolution and hence sensitivity to field gradients, resonance frequencies were determined with the smallest uncertainties of ±1.5 kHz in the Ramsey spectra performed at microwave frequencies. The broader features in the single-pulse Rabi spectra yielded uncertainties down to ±3.7 kHz.

IV. RESULTS

To determine absolute static magnetic-field strengths using atoms in circular Rydberg states, it was first necessary to characterize and where possible minimize electric fields in the measurement region. The procedure implemented to achieve this is presented below. This is followed by a description of the process employed to identify contributions from Doppler shifts and achieve absolute calibration. Finally, a one-dimensional absolute magnetic-field map is presented to demonstrate the capabilities of the technique.

A. Electric-field cancellation

To precisely measure magnetic fields along the axis of propagation of the atomic beam in Fig. 1(a), at each measurement position, i.e., at each value of t_μ, it was necessary to cancel stray electric fields and the motional Stark effect. These stray fields were caused by imperfections, adsorbates, and patch potentials on the surfaces of electrodes E1 and E2. The motional Stark effect [42], for which the effective motional electric field $\vec{F}_{\rm mot} = \vec{v} \times \vec{B}$, with $\vec{v}$ the velocity of the atoms and $\vec{B}$ the external magnetic field, was maximal in the geometry in which the experiments were performed since $\vec{v}$ is perpendicular to $\vec{B}$. However, because the atomic beam had a well-defined velocity and a narrow longitudinal velocity spread $\Delta v_z \simeq \pm 50$ m/s, the motional Stark effect could be compensated through the application of appropriate offset electric fields between E1 and E2 [32,43].

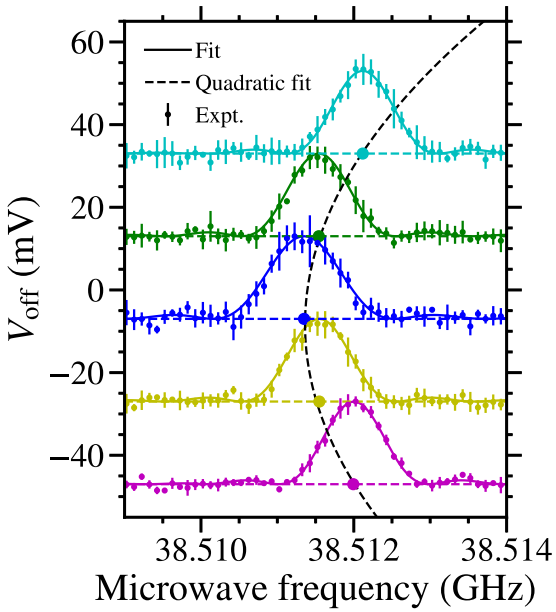

FIG. 4. Microwave spectra of the $|55c\rangle \rightarrow |56c\rangle$ transition in a magnetic field of approximately 1.6 mT (small data points). The spectral intensities, corresponding to the integrated $|56c\rangle$ electron signal, are normalized so that the intensity maximum in each spectrum is equal. The offset potential applied to electrode E2 when recording each spectrum is indicated on the left axis and represented by the vertical offset. The large points beneath each feature indicate the resonance frequency obtained from a least-squares fit of Eq. (5) (solid curves) to the experimental data. The quadratic function fit to these measured resonance frequencies to determine the offset potential required for optimal electric-field cancellation, in this case $V_{\rm off} = -8.52 \pm 0.11$ mV, is indicated by the black dashed curve.

The electric-field cancellation procedure involved recording single-pulse Rabi spectra of the $|55c\rangle \rightarrow |56c\rangle$ transition with a range of offset potentials applied to electrode E2. Examples of these can be seen in Fig. 4. For each of these measurements, the atoms were initially prepared in the $|55c\rangle$ state and a 1-μs-duration pulse of microwave radiation was applied at $t_\mu = 3.15$ μs while monitoring population transfer to the $|56c\rangle$ state. From these data, the Stark shift of the transition could be determined by fitting the Rabi line-shape function in Eq. (5) using least-squares methods. The corresponding resonance frequencies were determined to a minimum uncertainty of ±3.7 kHz and are indicated by the large solid points beneath each intensity maximum. In this figure, the spectra are normalized such that the intensity maximum of each fit function is equal, and each spectrum is offset on the vertical axis by an amount proportional to the value of $V_{\rm off}$. Each of these spectra represents the average of three consecutive loops over the measurement frequency range. Within each of these loops, the individual measurements at each microwave frequency (the average of 150 cycles of the experiment) were made in a random order to minimize systematic contributions from slow drifts in the experimental conditions.

The offset potential required to cancel the motional Stark effect and minimize electric fields in the x dimension in the measurement region was determined by fitting a quadratic function, reflecting the Stark shift of the $|55c\rangle \rightarrow |56c\rangle$ transition, to sets of resonance frequencies such as those associated with the spectra in Fig. 4 (black dashed curve). The value of $V_{\rm off}$ at the turning point of this function, in this example -8.52 ± 0.11 mV, was then considered the optimal cancellation potential and applied in the experiments when recording higher-resolution Ramsey spectra. With this cancellation potential applied to E2, stray electric fields acting in the x dimension were reduced to ±85 μV/cm.

B. Characterization of residual uncanceled electric fields

The geometry of the electrodes in the measurement region of the apparatus meant that the procedure described above only allowed cancellation of the motional Stark effect and static electric fields acting in the x dimension. The edges of electrodes E1 and E2 are far from the position of the atoms (greater than 35 mm in each of the y and z dimensions). However, weak uncanceled stray electric fields, including fringe fields, acting in these dimensions can persist. To determine absolute magnetic-field strengths from the spectra of circular-to-circular state transitions, it was necessary to account for contributions from these stray fields. This was done by first recording spectra of a single-photon electric dipole forbidden transition between two Rydberg states in a range of weak electric fields applied in the x dimension and from each measurement determining the amplitude of the observed spectral line. A linear least-squares fit could then be made to the dependence of this spectral intensity on the square of the offset potential $dV_{\rm off}$ applied to generate the fields, to extrapolate to zero intensity and determine the magnitude of the uncanceled fields [35,44]. For the precision required in the current experiments, this method is superior to determining the Stark shift of the absolute frequency of a microwave transition between Rydberg states because it is not affected by Doppler shifts.

The most convenient single-photon electric dipole forbidden transition to use to characterize residual stray electric fields in this way was that from the $1s56s\,^3S_1$ ($|56s\rangle$) level to the $1s57s\,^3S_1$ ($|57s\rangle$) level. This occurs at $\nu_{56s,57s} = 37.061\,950$ GHz in the absence of external fields. The $|56s\rangle$ state can be populated using the same excitation and electric-field-switching scheme as for circular state preparation, by making a small, approximately −75 mV/cm adjustment to the excitation electric field and changing the infrared laser frequency by +345 MHz. These changes caused minimal disturbance to the phase-space properties of the bunch of excited atoms and their environment. Examples of spectra of the $|56s\rangle \rightarrow |57s\rangle$ transition recorded in this way with a single pulse of microwave radiation applied at $t_\mu = 3.15$ μs and with a duration $\tau = 1$ μs are presented in Fig. 5(a). The Rabi line-shape function in Eq. (5) was fit to these data to extract the spectral intensity on resonance. For the weak fields employed in these measurements, the spectral intensity of the transition changes quadratically with the offset potential $dV_{\rm off}$. This can be seen from the blue points in Fig. 5(b). A line fit to these data using least-squares methods is shown as the red solid curve in this figure. Although the component of the field in the x dimension is minimized when $dV_{\rm off} = 0$ (see Fig. 4), for the conditions under which the spectra in Fig. 5 were recorded this is not commensurate with the transition exhibiting zero

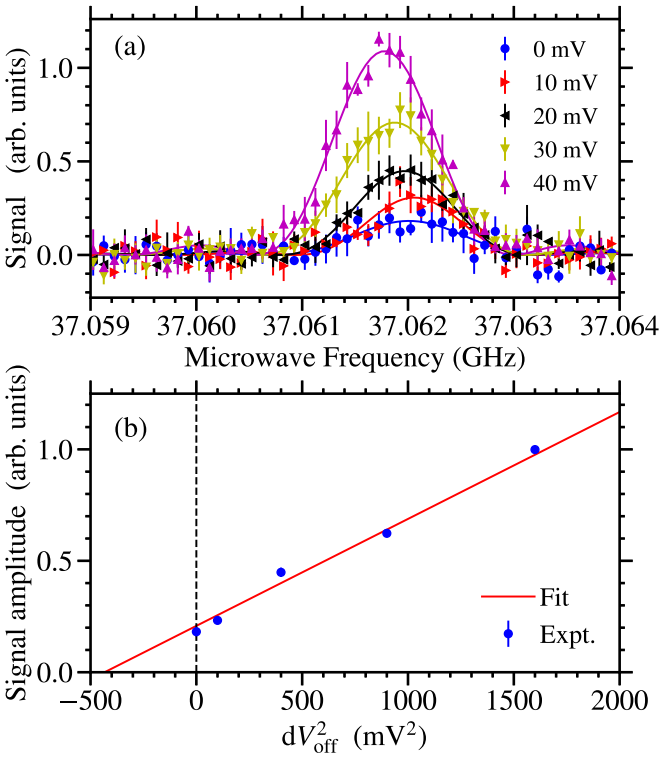

FIG. 5. (a) Single-photon electric dipole forbidden $|56s\rangle \rightarrow |57s\rangle$ transition recorded in weak electric fields acting in the x dimension and generated by applying the offset potentials dV_{off} indicated to E2. (b) Dependence of the measured spectral intensity in (a) on dV_{off}^2 (blue points). A linear least-squares fit to the experimental data is presented as the red solid curve.

spectral intensity. This is because of the presence of residual uncanceled electric fields in the y and z dimensions. The magnitudes of these fields were determined by linear extrapolation of the measured spectral intensities to the value of dV_{off}^2 for which the intensity reached zero. From the value of $dV_{off}^2 = 433.60 \pm 42.32$ (mV)^2, i.e., $dV_{off} = 20.82 \pm 1.02$ mV, at this intercept in the figure, and the 13.46-mm separation between E1 and E2, this yielded a residual uncanceled electric field in the y and z dimensions of 15.47 ± 0.75 mV/cm.

C. Radio-frequency spectroscopy

Further information on effects of electric fields in the measurement region, in particular those acting in the z dimension, parallel to the magnetic field was obtained by radio-frequency spectroscopy of the single-photon $\Delta n = 0$ and $\Delta m_\ell = -1$ transition from the $|55c\rangle$ state within the $n = 55$ manifold. In a 1.6-mT magnetic field, this transition occurs at a frequency close to 22 MHz. It was driven by an oscillating electric field linearly polarized perpendicular to the magnetic field by applying a sinusoidal perturbation to the potential on electrode E1. This transition is sensitive to Stark and Zeeman shifts, but because of the low frequency at which it occurs, and the geometry of the experimental apparatus first-order Doppler shifts are negligible. Population transfer in the measurements was monitored by depletion of the $|55c\rangle$ electron signal following pulsed-electric-field ionization. In the parallel electric

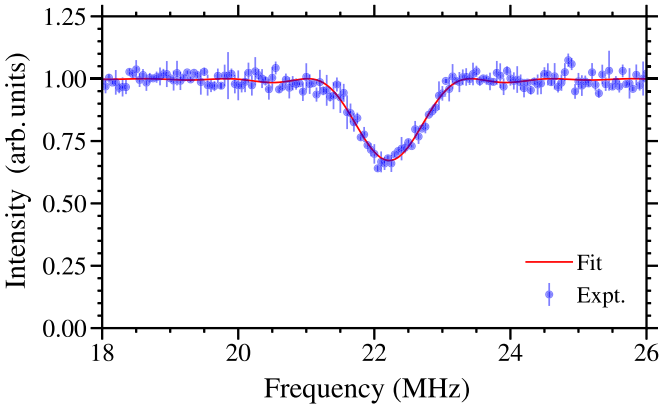

FIG. 6. Radio-frequency spectrum of the single-photon $\Delta n = 0$, $\Delta m_\ell = -1$ transition from the $|55c\rangle$ state. This spectrum was recorded in depletion with a $\tau = 1$ μs rf pulse applied to E1 at $t_{rf} = 3.15$ μs. The red solid curve represents a Rabi line-shape fit to the experimental data (points) using least-squares methods.

and magnetic fields of the detection region, atoms in the $|55c\rangle$ state ionized, i.e., the tunnel ionization rate exceeded 10^8 s^{-1}, in a field of approximately 98 V/cm. Because of the linear components to their Stark shifts in this configuration of fields, the ℓ-mixed $m_\ell = +53$ Stark states ionized in different fields, between 95 and 98 V/cm, which were on average lower than the ionization field of the $|55c\rangle$ state. These fields were sufficiently different from the ionization field of the $|55c\rangle$ state to allow detection of the rf transition to be carried out by monitoring the depletion of the $|55c\rangle$ electron signal.

An rf depletion spectrum, recorded for $t_\mu = 3.15$ μs using an rf pulse with a nominal duration of $\tau = 1$ μs, is presented in Fig. 6. The resonance frequency obtained by fitting the Rabi line-shape function to these data was $\nu_{rf} = 22.2188$ MHz $\pm$ 11.1 kHz. The FWHM resonance width determined through this fitting procedure was 834 ± 19 kHz. This corresponds to the Fourier transform limit of a rectangular pulse with a duration of 1.06 ± 0.03 μs.

This $\Delta m_\ell = -1$ transition to a state which is not circular has an enhanced sensitivity to stray electric fields oriented parallel to the background magnetic field, i.e., in the z dimension, when compared to the $|55c\rangle \rightarrow |56c\rangle$ transition. This is because of the static electric dipole moment, and hence linear Stark shift, of the $m_\ell = n - 2$ sublevel given by Eq. (4), in weak electric fields. Because of this behavior, if the residual uncanceled electric field of 15.47 mV/cm obtained from Fig. 5 had equal magnitude components in the x and z dimensions, i.e., $F_x = F_z = 10.94$ mV/cm, the spectrum in Fig. 6 would contain two features separated in frequency by 2.310 MHz. However, because only a single narrow resonance with a FWHM spectral width commensurate with that expected solely from the Fourier transform of the rf pulse is seen in Fig. 6, it is concluded that no significant spectral broadening occurred because of uncanceled electric fields acting in the z dimension. The uncertainty of approximately ± 20 kHz with which the measured FWHM was determined could therefore be used to place an upper bound on the electric field in this dimension of $F_z = 100$ μV/cm.

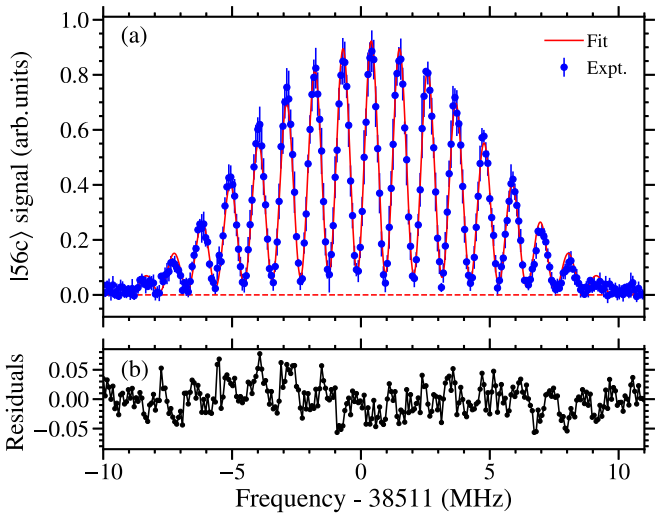

FIG. 7. (a) Ramsey spectrum of the $|55c\rangle \rightarrow |56c\rangle$ transition recorded for $t_\mu = 3.15$ μs in a magnetic field of approximately 1.6 mT. The Ramsey line-shape [Eq. (7)] fit to the experimental data using least-squares methods is displayed as the red solid curve. (b) Residuals resulting from the least-squares fit to the experimental data in (a).

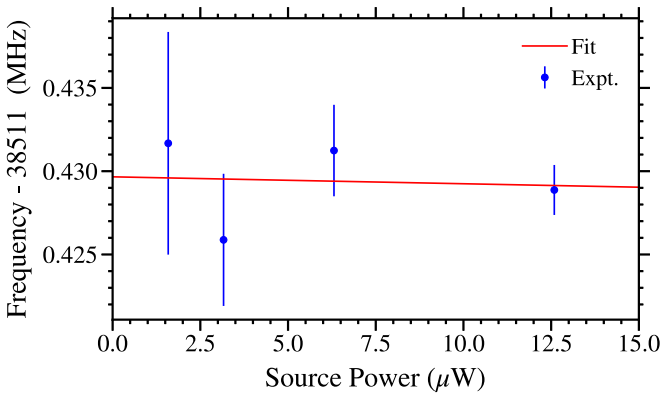

FIG. 8. Measured $|55c\rangle \rightarrow |56c\rangle$ transition frequencies recorded at $t_\mu = 3.15$ μs and a range of microwave source output powers (blue points). The red solid line fit to the experimental data using least-squares methods has a slope of -0.042 ± 0.386 MHz/μW.

Based on this interpretation of the data in Fig. 6, the dominant contribution from the residual uncanceled 15.47 mV/cm electric field obtained from the measurements of the single-photon electric dipole forbidden $|55s\rangle \rightarrow |56s\rangle$ transition in Fig. 5 must therefore act in the y dimension. The total stray electric field at the position of the atoms when $t_{\mu,\mathrm{rf}} = 3.15$ μs was therefore $\vec{F}_{\mathrm{stray}} = (\pm 85\ \mu\mathrm{V/cm}, 15.47 \pm 0.75\ \mathrm{mV/cm}, \pm 100\ \mu\mathrm{V/cm})$. The effect of the nonzero y component of this stray field on the $\Delta n = 0$ and $\Delta m_\ell = -1$ rf transition from the $|55c\rangle$ state can be accounted for using Eq. (2) to allow a determination of the magnetic-field strength with negligible contributions from Doppler shifts. This process yielded a magnetic-field strength of 1.5832 mT ± 900 nT. This magnetic-field strength and the residual uncanceled electric field in the y dimension of 15.47 ± 0.75 mV/cm were then used together with the expression in Eq. (2) and the $|55c\rangle \rightarrow |56c\rangle$ transition frequencies obtained from high-resolution Ramsey spectra to accurately determine Doppler shifts and perform absolute calibration of the Rydberg-atom magnetometer.

D. Ramsey spectroscopy of the $|55c\rangle \rightarrow |56c\rangle$ transition

Ramsey spectroscopy was performed at microwave frequencies to precisely measure the $|55c\rangle \rightarrow |56c\rangle$ transition frequency and determine with high relative precision and good spatial resolution the magnitude of magnetic fields at a range of positions in the apparatus. These measurements were implemented with pairs of $\tau = 100$ ns duration microwave pulses separated by a free-evolution time of $T_\mu = 800$ ns. To maximize the signal-to-noise ratio, the output power of the microwave source was set to achieve 80%–90% population transfer on resonance. A Ramsey spectrum recorded in this way for $t_\mu = 3.15$ μs is presented in Fig. 7(a).

To determine the $|55c\rangle \rightarrow |56c\rangle$ transition frequency from the spectrum in Fig. 7(a), the Ramsey line-shape function in Eq. (7) was fit to the experimental data using least-squares methods (red solid curve). The suitability of this line-shape function to describe the experimental data can be seen from the residuals in Fig. 7(b). These have a mean of -1.18×10^{-9} and a standard deviation of 0.0255. This process yielded a resonance frequency of $\nu_{55c,56c} = 38.511\,401\,8$ GHz ± 1.5 kHz and a coherence time of $T_{\mathrm{coh}} = 5.40 \pm 0.47$ μs. This finite coherence time was the source of the below-unity contrast in the Ramsey fringes seen most clearly at relative frequencies close to zero.

In the absence of stray electric fields, the ±1.5-kHz uncertainty in the $|55c\rangle \rightarrow |56c\rangle$ transition frequency obtained from the Ramsey spectrum in Fig. 7 would correspond to a relative uncertainty in magnetic-field strength of ±110 nT. However, in the presence of the residual uncanceled $F_y = 15.47 \pm 0.75$ V/cm electric field, this relative uncertainty increases to ±1.3 μT. To use spectra of the kind in Fig. 7 to precisely determine absolute magnetic-field strengths, it was also necessary to account for the systematic contributions from the Doppler effect. Comparison of the measured transition frequency with that expected for the $|55c\rangle \rightarrow |56c\rangle$ transition in the 1.5832-mT magnetic field determined without Doppler contributions by rf spectroscopy and the residual uncanceled electric field in the y dimension of 15.47 ± 0.75 mV/cm, yielded a Doppler shift of $\Delta\nu_{\mathrm{D}} = 50.91 \pm 21.65$ kHz. With this systematic correction and hence absolute calibration applied, magnetic fields were therefore determined by Ramsey spectroscopy of the $|55c\rangle \rightarrow |56c\rangle$ transition to an absolute precision of ±2.0 μT.

As a final test of the absolute calibration of this Rydberg-atom magnetometry scheme, a set of Ramsey spectra were recorded at $t_\mu = 3.15$ μs, with $\tau = 100$ ns, $T_\mu = 800$ ns, and a range of output powers of the microwave source to identify any systematic contributions from ac Stark shifts. The resulting dependence of the measured resonance frequency on the microwave power is displayed in Fig. 8. The high-precision Ramsey spectrum in Fig. 7(a) was recorded with a source output power of 12.5 μW (rightmost data point in

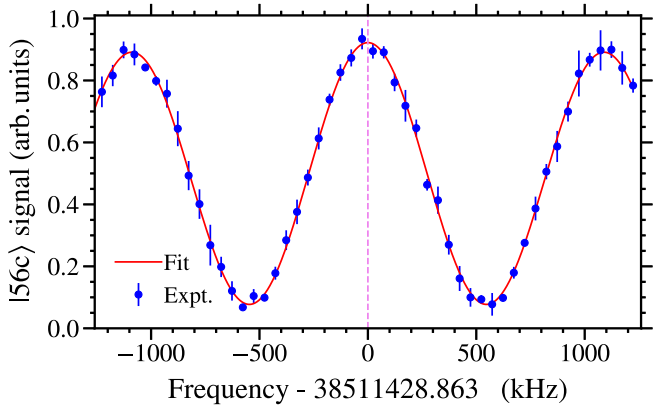

FIG. 9. Ramsey spectrum recorded at $t_\mu = 3.15$ μs over a reduced frequency range compared to that in Fig. 7, to determine the $|55c\rangle \rightarrow |56c\rangle$ transition frequency with high precision using only the central spectral fringes.

Fig. 8). A least-squares fit of a straight line to these data yielded a slope of -0.042 ± 0.386 MHz/μW. Since the ac Stark shift represented by this function, -0.5 ± 4.8 kHz, is consistent with zero, it is concluded that ac Stark shifts do not significantly affect the absolute precision of the magnetic-field determination under the current experimental conditions. Therefore, to ensure a maximal signal-to-noise ratio, for all further measurements discussed below the output power of the microwave source was set to 12.5 μW. This corresponded to an intensity of the microwave field at the position of the atoms of approximately 1.7×10^{-8} W/cm^2 as determined by time-domain measurements of Rabi oscillations.

E. Magnetic-field mapping

To map magnetic fields along the axis of propagation of the atomic beam, Ramsey spectra of the $|55c\rangle \rightarrow |56c\rangle$ transition were recorded for values of t_μ between 3.15 and 23.15 μs. Over this range of times, the position of the atoms extended in the y dimension from 8.55 mm to 41.27 mm from the position of laser photoexcitation [nominally the midpoint of the pair of solenoids; see Fig. 1(a)]. This set of measurements therefore allowed magnetic fields to be mapped over a distance of approximately 35 mm with a spatial resolution of ±0.87 mm.

To record the sets of Ramsey spectra required for magnetic-field mapping efficiently while maintaining high precision, it was sufficient to cover shorter frequency ranges than that in Fig. 7 but with slightly smaller frequency intervals between the measurement points. An example of such a shortened spectrum is seen in Fig. 9. This covers the frequency range around the central three fringes in Fig. 7(a). From the least-squares fit of Eq. (7) to these data, using the coherence time $T_{\rm coh} = 5.40$ μs obtained in Sec. IV D, resonance frequencies were determined to a precision of ±1.5 kHz. Spectra similar to that in Fig. 9 were subsequently recorded after cancellation of the motional Stark effect for each selected value of t_μ.

The one-dimensional map of the absolute magnetic-field strength obtained by following this procedure, with all corrections for residual stray electric fields and Doppler shifts accounted for, is presented as the blue points in Fig. 10. The uncertainty in the field at each individual measurement position is ±2.0 μT and smaller than the size of points. The ±0.87-mm spatial resolution, set by the longitudinal spread of the bunch of circular Rydberg atoms, is indicated by the horizontal bar associated with each point. Over the range of positions encompassed by the measurements, the field exhibits a quadratic dependence on the position in the y dimension. This is evident from the blue solid curve which represents a least-squares fit of such a function to the experimental data. The set of measurements in this map were made in a random order over the course of 8 h. Because the solenoids were not temperature stabilized, slow drifts in the magnetic field occurred. The deviations of the data points by more than the measurement uncertainty from the fit function are attributed to this slow time variation of the field.

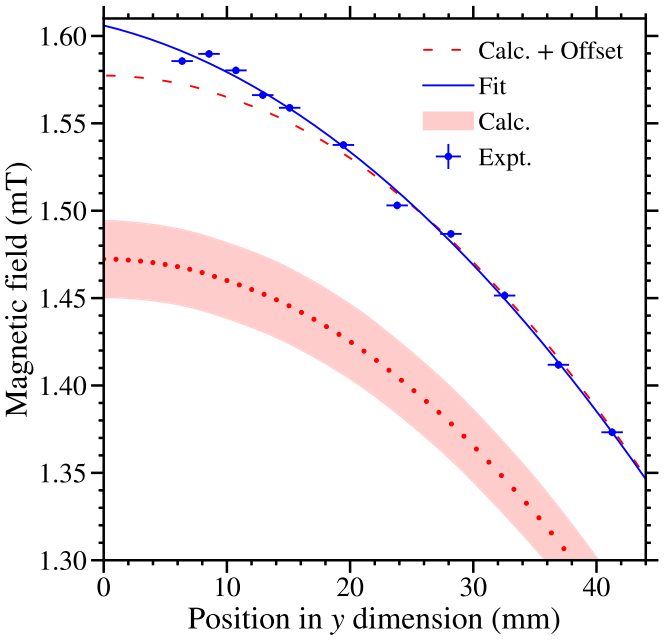

FIG. 10. One-dimensional map of the magnetic field on the axis of propagation of the atomic beam. The experimental data (blue points) have an absolute magnetic-field uncertainty of ±2.0 μT. The relative uncertainty in the measurement positions is ±0.87 mm. The blue solid curve represents a least-squares fit of a quadratic function to the data. The red shaded region corresponds to the result of a finite-element calculation of the magnetic field for the solenoid geometry used in the experiments. The red dashed curve is the mean-calculated field strength (red solid curve) offset by +105 μT (see the text for details).

The experimental data in Fig. 10 have been compared to the results of finite-element calculations for the solenoid geometry detailed in Sec. II. Upper and lower bounds on the calculated magnetic-field strength were determined from the uncertainties in the solenoid dimensions. These bounds are denoted by the red shaded band in the figure. The red dotted curve in the middle of this region represents the mean calculated field strength at each position.

In general, the measured magnetic-field distribution in Fig. 10 follows the form of the calculated distribution. The field is larger close to the middle of the solenoids where $y = 0$ and reduces quadratically with distance from this point. However, because stray magnetic fields were not actively canceled in the apparatus and the measurement region was not shielded from fields other than that to be measured, the finite-element calculations do not provide a complete picture of the magnetic environment. Consequently, the absolute magnetic-field strength can only be determined accurately from the experimental data.

The discrepancy between the results of the calculations and the experimental data can be estimated from the red dashed curve, which represents the mean calculated field distribution (red dotted curve) offset by $+105$ μT. Because the current in the solenoids was set to a nominal precision of approximately 10^{-4}, this discrepancy of more than 10^{-2} between the measured and calculated field strengths must be dominated by other sources. A contribution of $+45$ μT is attributed directly to the effect of the Earth's magnetic field. This was 49.01 μT in London, UK on 17th November 2022 when the experiments were performed and was directed at an angle of 24° with respect to the applied magnetic field in the z dimension in the apparatus [45]. The remaining $\sim 60 -$ μT difference is on the scale of fields measured using a Hall probe to originate from weakly magnetized components of the vacuum chamber and surrounding laboratory infrastructure.

From the ± 0.87-mm spatial resolution of the magnetic-field map in Fig. 10 and the ± 1.3-μT relative precision with which the magnetic fields were measured, it is concluded that magnetic-field gradients could be determined using this measurement scheme to a precision of ± 1.49 μT/mm over the minimal achievable baseline of 1.74 mm or ± 53 nT/mm over the maximal baseline of 35 mm covered in the experiments.

V. CONCLUSION

We have demonstrated the use of atoms in circular Rydberg states for (i) the absolute determination of static magnetic fields to a precision of ± 2.0 μT with a spatial resolution of ± 0.87 mm, (ii) the measurement of static magnetic-field gradients to a precision of ± 1.49 μT/mm (± 53 nT/mm) over a 1.75-mm (35-mm) baseline, and (iii) the measurement of the x, y, and z components of weak static electric fields to a precision of between ± 85 and ± 750 μV/cm. The uncertainty in the measured magnetic fields was dominated by contributions from residual uncanceled electric fields and Doppler shifts. Nevertheless, these results set a baseline standard for absolute static-field magnetometry, magnetic-field gradiometry, and vector electrometry with atoms in circular Rydberg states.

In the future, the measurement techniques described here could be extended to three-dimensional magnetic and electric-field mapping with the addition of an imaging MCP detector located on the axis of propagation of the atomic beam [46]. This will allow spatially resolved detection of electrons produced following state-selective pulsed electric-field ionization in the dimensions transverse to the beam propagation direction. To allow the reliable determination of circular Rydberg state populations by ionization in an electric field oriented parallel to the background magnetic field, such a measurement scheme will be most effectively implemented if the atomic beam is arranged to propagate along the axis of the solenoid(s) used to generate the magnetic field to be mapped.

Improvements in the absolute precision with which magnetic fields can be determined in these types of measurements will be obtained if stray electric fields are actively minimized in all three x, y, and z, spatial dimensions. The magnetic-field measurement precision in the work reported here approaches the limit associated with the inhomogeneity of the magnetic fields across the ensemble of excited Rydberg atoms. In a homogeneous field, the coherence time of $T_{\rm coh} = 5.40$ μs obtained from the measured Ramsey spectra would permit an improvement in measurement precision by a factor of at least 5. With appropriate electric-field control this would allow magnetic fields to be determined to a relative precision on the order of ± 10 nT. Future refinements and improved spatial resolution, particularly in more inhomogeneous fields, will benefit from the use of smaller bunches of atoms prepared by photoexcitation with more tightly focused nanosecond pulsed lasers and more slowly moving atomic beams. The latter can be generated by cooling the source. To maximize the measurement precision while maintaining short interrogation times, to allow good spatial resolution, the Ramsey spectroscopy technique could be implemented using the frequency offset separated oscillatory fields approach [47]. This has recently been very successfully employed at microwave frequencies for measurements of the $1s2p\,^3P_J$ fine structure in He [48] and the Lamb shift in atomic hydrogen [49].

The use of atoms in circular Rydberg states for mapping stronger magnetic fields, in excess of 0.1 T, could be performed with similar absolute precision at lower values of n, i.e., in the range from $n = 25$ to 30. This will ensure that diamagnetic contributions which scale with n^4 are minimal [50,51]. At these lower values of n the circular state lifetimes range from 0.9 to 2.1 ms and $\Delta n = +1$ circular-to-circular state transition frequencies range from 400 to 230 GHz. In a cryogenic environment, these lifetimes could allow high-precision measurements with a spatial resolution of 1 mm, over distances approaching 1 m.

With refinements of these kinds it is anticipated that the techniques presented here could be extended to allow absolute determination of static magnetic and electric fields to a precision of at least ± 100 nT and ± 10 μV/cm, respectively, with a spatial resolution approaching ± 100 μm. This set of specifications is well suited to the magnetometry, magnetic gradiometry, and vector electrometry requirements of hybrid cavity QED experiments with Rydberg atoms and superconducting circuits, tests of bound state QED in one- and two-electron atoms and molecules, tests of the weak equivalence principle by electric Rydberg-atom interferometry with positronium atoms, and experiments to determine the absolute neutrino mass by CRES.

ACKNOWLEDGMENTS

This work was supported by the UK Science and Technology Facilities Research Council through the Quantum Technologies for Neutrino Mass project (Grant No. ST/T006439/1).

[1] E. K. Dietsche, A. Larrouy, S. Haroche, J. M. Raimond, M. Brune, and S. Gleyzes, High-sensitivity magnetometry with a single atom in a superposition of two circular Rydberg states, Nat. Phys. **15**, 326 (2019).

[2] A. Osterwalder and F. Merkt, Using High Rydberg States as Electric Field Sensors, Phys. Rev. Lett. **82**, 1831 (1999).

[3] H. Fan, S. Kumar, J. Sedlacek, H. Kübler, S. Karimkashi, and J. P. Shaffer, Atom based RF electric field sensing, J. Phys. B **48**, 202001 (2015).

[4] M. T. Simons, A. B. Artusio-Glimpse, A. K. Robinson, N. Prajapati, and C. L. Holloway, Rydberg atom-based sensors for radio-frequency electric field metrology, sensing, and communications, Measurement: Sensors **18**, 100273 (2021).

[5] R. G. Hulet and D. Kleppner, Rydberg Atoms in "Circular" States, Phys. Rev. Lett. **51**, 1430 (1983).

[6] J. Liang, M. Gross, P. Goy, and S. Haroche, Circular Rydberg-state spectroscopy, Phys. Rev. A **33**, 4437 (1986).

[7] S. Gleyzes, S. Kuhr, C. Guerlin, J. Bernu, S. Deléglise, U. Busk Hoff, M. Brune, J.-M. Raimond, and S. Haroche, Quantum jumps of light recording the birth and death of a photon in a cavity, Nature (London) **446**, 297 (2007).

[8] S. Haroche, Nobel Lecture: Controlling photons in a box and exploring the quantum to classical boundary, Rev. Mod. Phys. **85**, 1083 (2013).

[9] J. Hare, A. Nussenzweig, C. Gabbanini, M. Weidemuller, P. Goy, M. Gross, and S. Haroche, Toward a Rydberg constant measurement on circular atoms, IEEE Trans. Instrum. Meas. **42**, 331 (1993).

[10] J. De Vries, A precision millimeter-wave measurement of the Rydberg frequency, Ph.D. thesis, MIT, 2001.

[11] A. Ramos, K. Moore, and G. Raithel, Measuring the Rydberg constant using circular Rydberg atoms in an intensity-modulated optical lattice, Phys. Rev. A **96**, 032513 (2017).

[12] A. Facon, E.-K. Dietsche, D. Grosso, S. Haroche, J.-M. Raimond, M. Brune, and S. Gleyzes, A sensitive electrometer based on a Rydberg atom in a Schrödinger-cat state, Nature (London) **535**, 262 (2016).

[13] J. E. Palmer and S. D. Hogan, Electric Rydberg-Atom Interferometry, Phys. Rev. Lett. **122**, 250404 (2019).

[14] T. L. Nguyen, J. M. Raimond, C. Sayrin, R. Cortiñas, T. Cantat-Moltrecht, F. Assemat, I. Dotsenko, S. Gleyzes, S. Haroche, G. Roux, T. Jolicoeur, and M. Brune, Towards Quantum Simulation with Circular Rydberg Atoms, Phys. Rev. X **8**, 011032 (2018).

[15] A. A. Morgan and S. D. Hogan, Coupling Rydberg Atoms to Microwave Fields in a Superconducting Coplanar Waveguide Resonator, Phys. Rev. Lett. **124**, 193604 (2020).

[16] M. Kaiser, C. Glaser, L. Y. Ley, J. Grimmel, H. Hattermann, D. Bothner, D. Koelle, R. Kleiner, D. Petrosyan, A. Günther, and J. Fortágh, Cavity-driven Rabi oscillations between Rydberg states of atoms trapped on a superconducting atom chip, Phys. Rev. Res. **4**, 013207 (2022).

[17] F. Biraben, Spectroscopy of atomic hydrogen. How is the Rydberg constant determined? Eur. Phys. J. Spec. Top. **172** 109 (2009).

[18] S. Scheidegger and F. Merkt, Spectroscopy of highly excited states of the hydrogen atom, Chimia **74**, 285 (2020).

[19] N. Hölsch, M. Beyer, E. J. Salumbides, K. S. E. Eikema, W. Ubachs, C. Jungen, and F. Merkt, Benchmarking Theory with an Improved Measurement of the Ionization and Dissociation Energies of H_2, Phys. Rev. Lett. **122**, 103002 (2019).

[20] M. Ahmadi, B. X. R. Alves, C. J. Baker, W. Bertsche, A. Capra, C. Carruth, C. L. Cesar, M. Charlton, S. Cohen, R. Collister, S. Eriksson, A. Evans, N. Evetts, J. Fajans, T. Friesen, M. C. Fujiwara, D. R. Gill, J. S. Hangst, W. N. Hardy, M. E. Hayden *et al.*, Observation of the 1S–2P Lyman-α transition in antihydrogen, Nature (London) **561**, 211 (2018).

[21] L. Gurung, T. J. Babij, S. D. Hogan, and D. B. Cassidy, Precision Microwave Spectroscopy of the Positronium $n = 2$ Fine Structure, Phys. Rev. Lett. **125**, 073002 (2020).

[22] D. B. Cassidy and S. D. Hogan, Atom control and gravity measurements using Rydberg positronium, Int. J. Mod. Phys. Conf. Ser. **30**, 1460259 (2014).

[23] G. S. Adkins, D. B. Cassidy, and J. Pérez-Ríos, Precision spectroscopy of positronium: Testing bound-state QED theory and the search for physics beyond the Standard Model, Phys. Rep. **975**, 1 (2022).

[24] B. Monreal and J. A. Formaggio, Relativistic cyclotron radiation detection of tritium decay electrons as a new technique for measuring the neutrino mass, Phys. Rev. D **80**, 051301(R) (2009).

[25] D. M. Asner, R. F. Bradley, L. de Viveiros, P. J. Doe, J. L. Fernandes, M. Fertl, E. C. Finn, J. A. Formaggio, D. Furse, A. M. Jones, J. N. Kofron, B. H. LaRoque, M. Leber, E. L. McBride, M. L. Miller, P. Mohanmurthy, B. Monreal, N. S. Oblath, R. G. H. Robertson, L. J. Rosenberg *et al.*, Single-Electron Detection and Spectroscopy via Relativistic Cyclotron Radiation, Phys. Rev. Lett. **114**, 162501 (2015).

[26] H. Hattermann, M. Mack, F. Karlewski, F. Jessen, D. Cano, and J. Fortágh, Detrimental adsorbate fields in experiments with cold Rydberg gases near surfaces, Phys. Rev. A **86**, 022511 (2012).

[27] M. Farooq, T. Chupp, J. Grange, A. Tewsley-Booth, D. Flay, D. Kawall, N. Sachdeva, and P. Winter, Absolute Magnetometry with ^{3}He, Phys. Rev. Lett. **124**, 223001 (2020).

[28] T. Halfmann, J. Koensgen, and K. Bergmann, A source for a high-intensity pulsed beam of metastable helium atoms, Meas. Sci. Technol. **11**, 1510 (2000).

[29] S. D. Hogan, Y. Houston, and B. Wei, Laser photoexcitation of Rydberg states in helium with $n > 400$, J. Phys. B **51**, 145002 (2018).

[30] D. Delande and J. C. Gay, A new method for producing circular Rydberg states, Europhys. Lett. **5**, 303 (1988).

[31] R. Lutwak, J. Holley, P. P. Chang, S. Paine, D. Kleppner, and T. Ducas, Circular states of atomic hydrogen, Phys. Rev. A **56**, 1443 (1997).

[32] V. Zhelyazkova and S. D. Hogan, Preparation of circular Rydberg states in helium using the crossed-fields method, Phys. Rev. A **94**, 023415 (2016).

[33] R. J. Damburg and V. V. Kolosov, A hydrogen atom in a uniform electric field. III, J. Phys. B **12**, 2637 (1979).

[34] G. W. F. Drake, High precision theory of atomic helium, Phys. Scr. **T83**, 83 (1999).

[35] A. Deller and S. D. Hogan, Microwave spectroscopy of the $1snp\,^3P_J$ fine structure of high Rydberg states in ^{4}He, Phys. Rev. A **97**, 012505 (2018).

[36] W. Pauli, Über das wasserstoffspektrum vom standpunkt der neuen quantenmechanik, Z. Phys. **36**, 336 (1926).

[37] R. J. Damburg and V. V. Kolosov, in *Rydberg States of Atoms and Molecules*, edited by R. F. Stebbings and F. B. Dunning (Cambridge University Press, Cambridge, 1983).

[38] H. A. Bethe and E. E. Salpeter, *Quantum Mechanics of One- and Two-Electron Atoms* (Springer, Berlin, 1957).

[39] M. J. Englefield, *Group Theory and the Coulomb Problem* (Wiley, New York, 1972).

[40] L. Allen and J. H. Eberly, *Optical Resonance and Two-Level Atoms* (Dover, New York, 1987).

[41] C. J. Foot, *Atomic Physics* (Oxford University Press, Oxford, 2004).

[42] H. Crosswhite, U. Fano, K. T. Lu, and A. R. P. Rau, Motional Stark Effect on Li Vapor Photoabsorption in High Magnetic Fields, Phys. Rev. Lett. **42**, 963 (1979).

[43] R. Elliott, G. Droungas, and J.-P. Connerade, Active cancellation of the motional Stark effect in the diamagnetic spectrum of Ba, J. Phys. B **28**, L537 (1995).

[44] J. Lee, J. Nunkaew, and T. F. Gallagher, Microwave spectroscopy of the cold rubidium $(n+1)\,d_{5/2} \rightarrow ng$ and nh transitions, Phys. Rev. A **94**, 022505 (2016).

[45] NOAA National Centers for Environmental Information, https://ngdc.noaa.gov/geomag-web/ (2023).

[46] T. Thiele, J. Deiglmayr, M. Stammeier, J.-A. Agner, H. Schmutz, F. Merkt, and A. Wallraff, Imaging electric fields in the vicinity of cryogenic surfaces using Rydberg atoms, Phys. Rev. A **92**, 063425 (2015).

[47] A. C. Vutha and E. A. Hessels, Frequency-offset separated oscillatory fields, Phys. Rev. A **92**, 052504 (2015).

[48] K. Kato, T. D. G. Skinner, and E. A. Hessels, Ultrahigh-Precision Measurement of the $n = 2$ Triplet P Fine Structure of Atomic Helium Using Frequency-Offset Separated Oscillatory Fields, Phys. Rev. Lett. **121**, 143002 (2018).

[49] N. Bezginov, T. Valdez, M. Horbatsch, A. Marsman, A. C. Vutha, and E. A. Hessels, A measurement of the atomic hydrogen Lamb shift and the proton charge radius, Science **365**, 1007 (2019).

[50] F. A. Jenkins and E. Segrè, The quadratic Zeeman effect, Phys. Rev. **55**, 52 (1939).

[51] W. R. S. Garton and F. S. Tomkins, Diamagnetic Zeeman effect and magnetic configuration mixing in long spectral series of Ba I, Astrophys. J. **158**, 839 (1969).